The Astrophysical Journal Letters, 940:L12 (8pp), 2022 November 20 https://doi.org/10.3847/2041-8213/ac9dfd
© 2022. The Author(s). Published by the American Astronomical Society.
OPEN ACCESS

Spectroscopic and Imaging Observations of Spatially Extended Magnetic Reconnection in the Splitting of a Solar Filament Structure

Huidong Hu[1], Ying D. Liu[1,2], Lakshmi Pradeep Chitta[3], Hardi Peter[3], and Mingde Ding[4,5]
[1] State Key Laboratory of Space Weather, National Space Science Center, Chinese Academy of Sciences, Beijing 100190, People's Republic of China
huhd@nssc.ac.cn, liuxying@swl.ac.cn
[2] University of Chinese Academy of Sciences, Beijing 100049, People's Republic of China
[3] Max Planck Institute for Solar System Research, Göttingen D-37077, Germany
[4] School of Astronomy and Space Science, Nanjing University, Nanjing 210023, People's Republic of China
[5] Key Laboratory for Modern Astronomy and Astrophysics (Nanjing University), Ministry of Education, Nanjing 210023, People's Republic of China
Received 2022 August 14; revised 2022 October 18; accepted 2022 October 27; published 2022 November 16

Abstract

On the Sun, Doppler shifts of bidirectional outflows from the magnetic-reconnection site have been found only in confined regions through spectroscopic observations. Without spatially resolved spectroscopic observations across an extended region, the distribution of reconnection and its outflows in the solar atmosphere cannot be made clear. Magnetic reconnection is thought to cause the splitting of filament structures, but unambiguous evidence has been elusive. Here we report spectroscopic and imaging analysis of a magnetic-reconnection event on the Sun, using high-resolution data from the Interface Region Imaging Spectrograph and the Solar Dynamics Observatory. Our findings reveal that the reconnection region extends to an unprecedented length of no less than 14,000 km. The reconnection splits a filament structure into two branches, and the upper branch erupts eventually. Doppler shifts indicate clear bidirectional outflows of $\sim$100 km s^{-1}, which decelerate beyond the reconnection site. Differential-emission-measure analysis reveals that in the reconnection region the temperature reaches over 10 MK and the thermal energy is much larger than the kinetic energy. This Letter provides definite spectroscopic evidence for the splitting of a solar filament by magnetic reconnection in an extended region.

Unified Astronomy Thesaurus concepts: Solar magnetic reconnection (1504); Solar filaments (1495); Solar filament eruptions (1981)

Supporting material: animation

1. Introduction

Magnetic reconnection is a process that changes magnetic topology and converts magnetic energy to plasma kinetic energy, which exists in laboratory and astrophysical plasmas (Zweibel & Yamada 2009). On the Sun, reconnection can contribute to eruptions (e.g., Lin et al. 2004), acceleration of energetic particles (e.g., Goldstein et al. 1986), and coronal heating (e.g., Antolin et al. 2021).

One indicator of magnetic reconnection is the Doppler effect of the reconnection outflows (e.g., Innes et al. 1997; Hong et al. 2016; Polito et al. 2018). Blue- and redshifts of bidirectional reconnection outflows are observed only in confined regions (e.g., Chifor et al. 2008; Tian et al. 2018; Ortiz et al. 2020). Spectroscopic observations suggest that small-scale reconnection can drive small jets of multiple temperatures (e.g., Chifor et al. 2008; Li et al. 2018). Imaging and spectroscopy reveal bidirectional outflows of reconnection that can heat small pockets of cool plasma in the photosphere (Peter et al. 2014). Doppler shifts of downward flows from the reconnection current sheet are disclosed in the late stage of an eruptive flare on the solar limb (French et al. 2020), where the eruption is associated with a global coronal wave (e.g., Hu et al. 2019). Spatially resolved spectroscopic observations covering extended regions in the solar atmosphere are rare, and thus the distribution of reconnection outflows and thermal properties on the Sun is unclear.

Original content from this work may be used under the terms of the Creative Commons Attribution 4.0 licence. Any further distribution of this work must maintain attribution to the author(s) and the title of the work, journal citation and DOI.

Models suggest that magnetic reconnection can occur internally in a filament structure and is associated with the splitting and/or partial eruption of the filament structure (e.g., Gilbert et al. 2001; Gibson & Fan 2006; Kliem et al. 2014). Imaging observations also indicate internal reconnection related to the splitting and partial eruption of a filament (e.g., Liu et al. 2008; Tripathi et al. 2009; Cheng et al. 2018). In a "double-decker" system that consists of two vertically separated filament branches, magnetic reconnection between the two branches can destabilize the upper branch and cause a partial eruption (Liu et al. 2012; Kliem et al. 2014). Doppler shifts of bidirectional outflows, as a clear indicator of reconnection in solar filament splitting, have not been detected in spectroscopic observations. Therefore, definite evidence for reconnection in the splitting of a solar filament has been elusive.

In this Letter, we report a magnetic-reconnection event that causes the splitting of a solar filament structure, based on spatially resolved spectroscopic data from the Interface Region Imaging Spectrograph (IRIS; De Pontieu et al. 2014a) and images from the Solar Dynamics Observatory (SDO; Pesnell et al. 2012). An overview of the filament splitting is described in Section 2. The spectroscopic results of the reconnection are delivered in Section 3. The temperature and the energy are estimated in Section 4. The investigation is concluded and discussed in Section 5. The reconnection is unique in that Doppler shifts of its bidirectional outflows are observed in an unprecedented extended region on the Sun. Our observations present clear spectroscopic evidence for the splitting of a solar filament induced by magnetic reconnection.

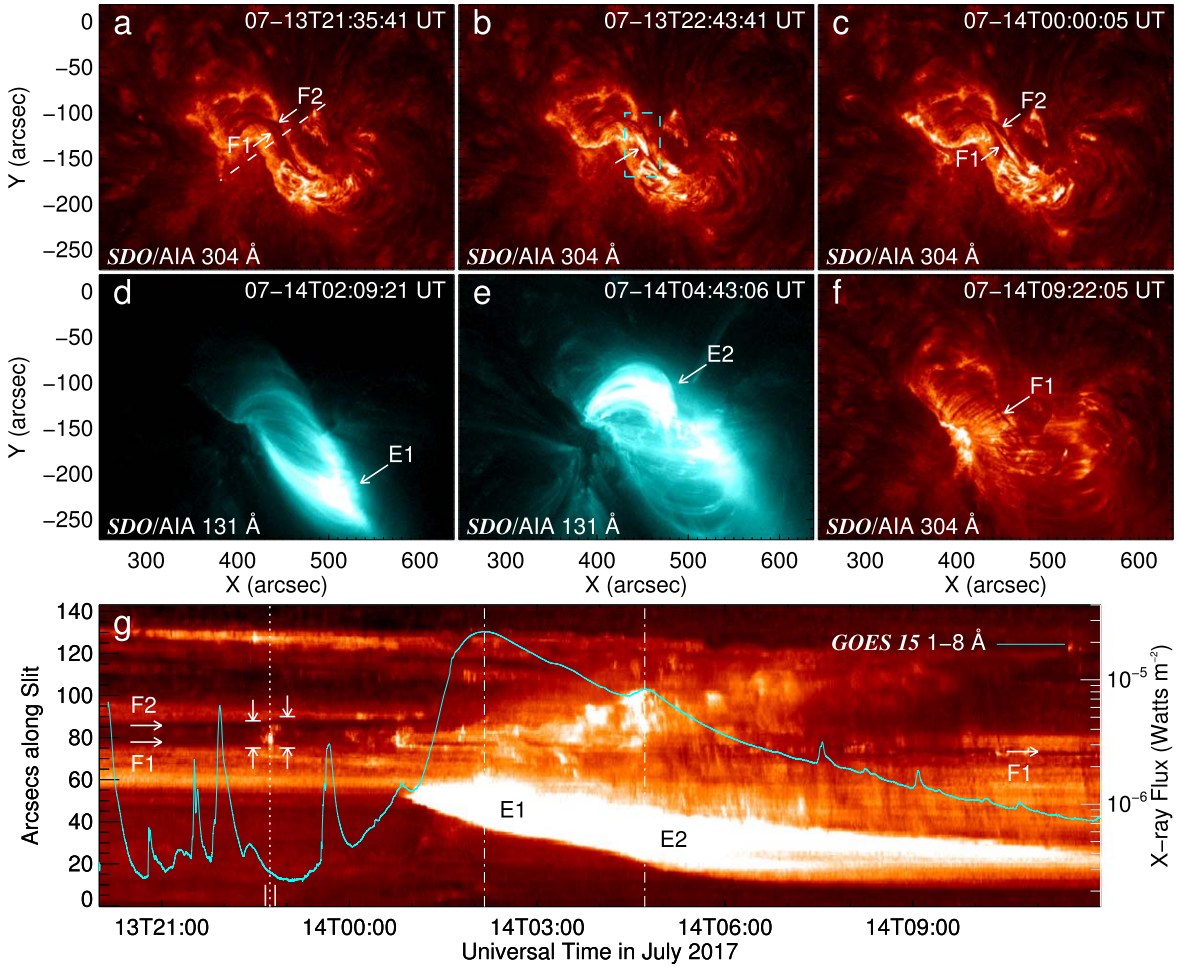

Figure 1. Splitting and partial eruption of the filament structure. (a)-(f) Images of SDO/AIA 304 Å ((a)–(c), (f)) and 131 Å ((d)–(e)). (g) Time–distance profile created by stacking AIA 304 Å images along the dashed line in (a), overlaid with GOES-15 1–8 Å X-ray flux in cyan color. The field of views (FOVs) of (a)–(f) are the same, whose coordinates are differentially rotated and are aligned to those of (b). "F1" and "F2" in (a), (c), (f), and (g) indicate the lower and upper filament branches, respectively. In (b) the arrow marks a brightening region between the two branches signifying the splitting. "E1" and "E2" in (d)–(e) denote two flares associated with the partial eruption. In (g) the dotted line on the left indicates the approximate time of the splitting, and the nearby two pairs of arrows illustrate the total width of the two filament branches before and after the splitting; the two dashed–dotted lines mark the times of the X-ray flux peaks of flares "E1" and "E2." The dashed rectangle in (b) represents the FOV of the IRIS raster scan displayed in Figures 2(c)–(e), and the two short vertical bars in (g) denote that the duration of the raster scan that overlaps the splitting. An animation for (a)–(c) is available, which begins at 07-13T22:00 UT and ends at 07-14T06:00 UT. The lines, arrows, and other annotations are removed in the animation. The real-time animation duration is ∼34 s.

(An animation of this figure is available.)

2. Observations and Overview

A filament structure in solar Active Region 12665 split and erupted on 2017 July 14. It produced a coronal mass ejection and an M 2.4 class flare with a flux peak at 02:09 UT (Jing et al. 2021). The Atmospheric Imaging Assembly (AIA; Lemen et al. 2012) on board SDO has observed the evolution of the filament structure. The AIA imaging data cadence and spatial resolution are 12 s and 0.″6, respectively. Figure 1 and the animation present the imaging observations from SDO/AIA. Figure 1(a) shows two contiguous filament branches (noted with "F1" and "F2" respectively), and Figure 1(b) displays a 304 Å brightening between the two branches. After the brightening, the two filament branches are separated (Figure 1(c)), and their total width increases by ∼2″ (Figure 1(g)). As shown in Figure 1(a)–(c), the north leg of "F2" crosses over "F1" from the west and is rooted in the south of "F1." This indicates that "F2" is higher than "F1," and otherwise their north legs will intersect. AIA 131 Å images in Figure 1(d)–(e) illustrate two flares corresponding to the two X-ray flux peaks in Figure 1(g). The flares indicate two eruptions of the filament structure. The lower branch ("F1" in Figure 1(f)–(g)), as part of the filament structure, survives the eruptions. These observations reveal that the filament structure is split into two branches. Although "F2" may not be exactly above "F1," the filament structure resembles a "double-decker" geometry (Liu et al. 2012). Afterwards, the structure undergoes a partial eruption by ejecting the upper filament branch "F2".

Four very large dense 400-step rasters are taken by IRIS, which scanned the leading polarity region of Active Region 12665 from 22:39 UT on 2017 July 13 to 00:56 UT on 2017 July 14. Each raster consists of 400 slits with a step size of 0.″35 and a pixel size of 0.″33. The step cadence is 5 s with an exposure time of 4 s, and the spectral resolution is 0.05 Å for the scan. We use the calibrated level 2 data with dark current subtraction, flat field, and geometrical corrections applied (De Pontieu et al. 2014a). The first of the four rasters covers the filament splitting spatially and temporally, which is analyzed in this study. The scan period is 22:39–23:13 UT on 2017 July 13,

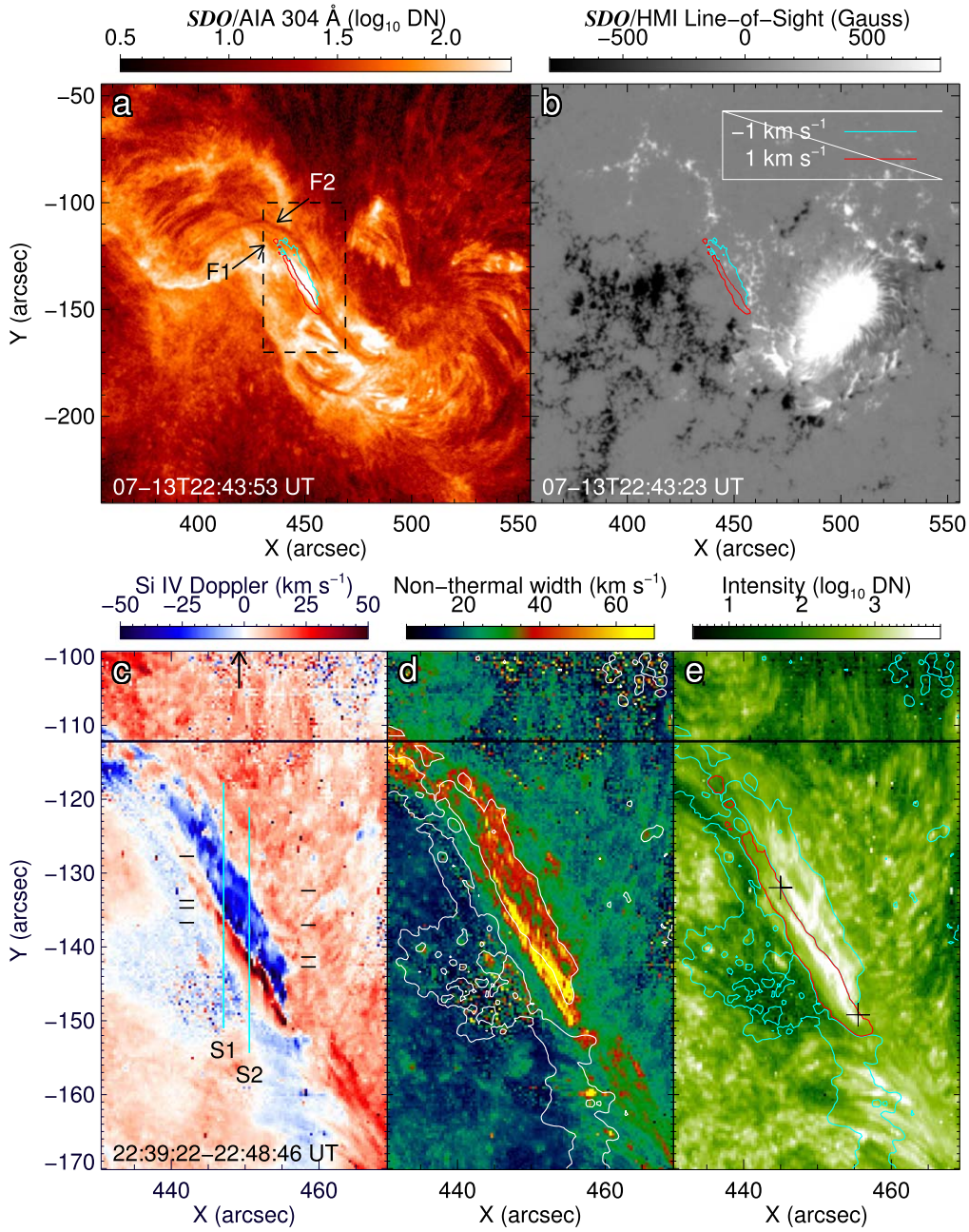

Figure 2. Magnetic reconnection in the filament splitting. (a) SDO/AIA 304 Å image showing the brightening region between the two filament branches. (b) SDO/HMI line-of-sight magnetogram of the active region. (c)–(e) Doppler map, nonthermal width, and intensity (in digital numbers, DN) derived from a single Gaussian fitting of Si IV 1393.755 Å line in the IRIS raster scan. Red contours in (a)–(b) and (e) are of 1 km s^{-1} redshift surrounding the brightening region. Cyan contours in (a)–(b) and (e), and white contours in (d) are of -1 km s^{-1} blueshift. The distance between the two crosses ("+") in (e) is $\sim 20''$ and represents the length of the reconnection region. In (a) the rectangle denotes the field of view (FOV) of the IRIS scan; "F1," "F2," and the arrows are similar to those in Figure 1(a). In (c) the two cyan slits "S1" and "S2" indicate where the spectra are displayed in Figure 3(a)–(b); the black dashes denote where on the slits the line profiles are plotted in Figure 3(c)–(d); the time range is the duration of the IRIS raster scan for the FOV; the arrow points to the scan slit whose observation time is the closest to that of the SDO/AIA image in (a). The horizontal line near $-110''$ in (c)-(e) is a fiducial line.

and the field of view is $140'' \times 174''$ centered at $(500'', -150'')$. To highlight the filament splitting, only a subfield of the raster ($39'' \times 70''$ centered at $(450'', -135'')$) is investigated in detail. The field of view of the subfield raster is marked in Figure 1(b).

3. High-resolution Spectroscopic Results

The filament splitting was captured on a rare occasion with the IRIS raster scan. We have adjusted the coordinates of the IRIS raster map by cross-correlating an IRIS Mg II k wing image and an AIA 1700 Å image (Chen et al. 2019). The Doppler velocity, nonthermal width, and intensity in Figure 2 are obtained by fitting Si IV 1393.755 Å line profiles with a single Gaussian function (Peter 2010). The Doppler velocity is then calibrated by removing the Doppler shift of averaged Fe II 1392.817 Å line (Tian et al. 2018). The nonthermal width is calculated by subtracting the thermal and instrumental broadening from the single Gaussian fitted width at $1/e$ of the peak intensity. The above processes are described in Appendix A. Neighboring large blue- and redshifts of $\gtrsim$50 km s^{-1} in the

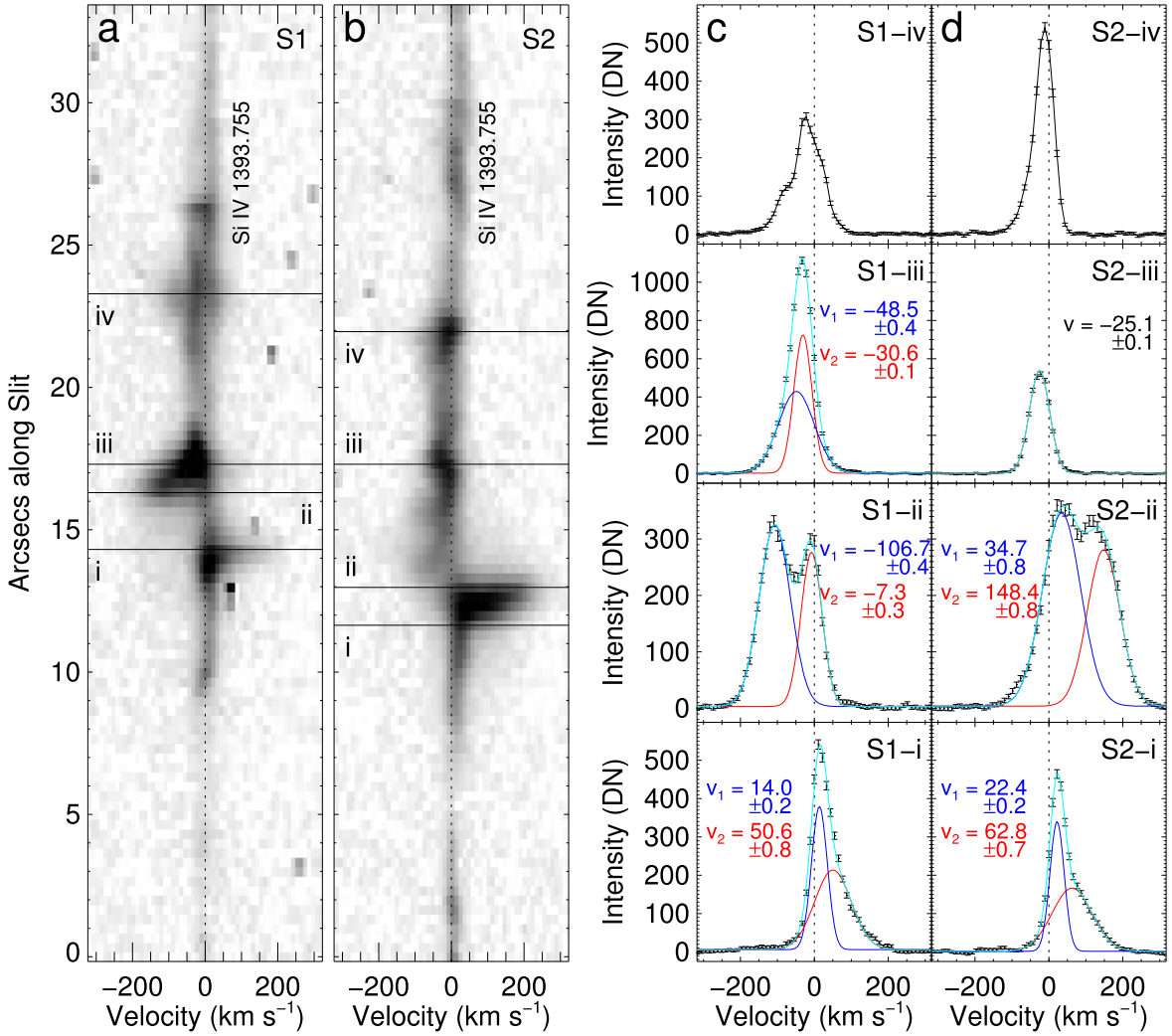

Figure 3. Spectra of the bidirectional outflows from the reconnection site. (a)–(b) Si IV 1393.755 Å line spectra on slits "S1–2" defined in Figure 2(c). The horizontal lines "i–iv" on each slit are corresponding to the dashes in Figure 2(c). (c)–(d) Line profiles in positions "i–iv" on "S1–2," and their double Gaussian fits for "i–iii" (but single Gaussian fit for "S2-iii"). The zero velocities are set to the rest wavelengths of Si IV 1393.755 Å. The black curves are the observed profiles; the cyan curves represent the total fits; the red and blue curves plot the two Gaussian components; the component velocities and their 1σ errors are given in kilometers per second.

brightening region of 304 Å between the two filament branches are revealed. For the Si IV 1393.755 Å line, the Doppler shifts spatially correspond to large nonthermal widths and enhanced intensities (brightening), and are also near the magnetic polarity inversion line (see the SDO Helioseismic and Magnetic Imager (HMI; Scherrer et al. 2012) magnetogram in Figure 2(b)). This is consistent with the observation that a filament is located at and parallel to a polarity inversion line (a boundary between opposite-polarity magnetic fields; Martin 1998). Doppler shift of Si IV line is one of the spectroscopic signatures of the bidirectional outflows of magnetic reconnection in the lower solar atmosphere (Peter et al. 2014). The nonthermal broadening could be explained by magnetic-reconnection induced turbulence or by the velocity dispersion in the outflows (e.g., Antonucci et al. 1986; Gordovskyy et al. 2016). The brightening of 304 Å and Si IV 1393.755 Å, between the two filament branches, indicates the hot plasma heated by magnetic reconnection (Li et al. 2018; Antolin et al. 2021). The SDO/AIA and IRIS observations have revealed the magnetic reconnection that occurs inside the filament structure and splits the structure into two branches. The length of the interface between the adjoining large blue- and redshifts, where the reconnection site is located, is estimated to be ∼20″ (between the two crosses in Figure 2(e)). The length is corresponding to ∼14,000 km on the Sun if it is measured at the disk center. IRIS took 150 s to scan the reconnection region. The 304 Å brightening lasts about 10 minutes, but it is not associated with an enhancement of X-ray flux (Figure 1(g)). This suggests that the reconnection in the filament splitting releases much lower energy than the reconnection during the filament eruption. The order of magnitude of the energy will be estimated in Section 4.

We further investigate the spectra and profiles of Si IV 1393.755 Å line on slits "S1" and "S2" specified in Figure 2(c). As displayed in Figure 3, both blueshift and its counterpart redshift are detected on each slit, between which the magnetic-reconnection site is located. The overall line width decreases notably on the blueshift side away from the reconnection site on "S1," and on the redshift side on "S2" (Figures 3(a)–(b)). These indicate that the velocities projected to the line of sight decrease after the bidirectional outflows have left the reconnection site. Line profiles near the reconnection site are asymmetric or double-peaked, which cannot be fitted well with a single Gaussian function. A κ distribution can be used to fit profiles with enhanced wings (e.g., Dudík et al. 2017). A

double Gaussian function is also applicable to fit the major velocity components of profiles with asymmetric wings and especially with double peaks (e.g., Peter 2010; Hong et al. 2016; Ortiz et al. 2020). In this study, a double Gaussian fitting (see Appendix A) is applied to line profiles at "i–iii" on "S1" and at "i–ii" on "S2" (but single Gaussian fitting for "S2-iii"; see Figure 3(c)-(d)). Separate double Gaussian components are fitted near the reconnection site on the two slits. A blueshift component greater than 100 km s^{-1} at "S1-ii" and a redshift component of nearly 150 km s^{-1} at "S2-ii" are obtained. Beyond the reconnection site, the blueshift decreases obviously to ~48 km s^{-1} at "S1-iii" and the redshift is reduced noticeably to ~62 km s^{-1} at "S2-i." These confirm that both the upward and downward outflows decelerate remarkably after they have left the reconnection site. We can also see line broadening, at "S1-iv" and "S2-iv," several arcseconds from the reconnection site on the blue wing, which may be a signature of turbulence (Jeffrey et al. 2018; Chitta & Lazarian 2020). The turbulence can be induced when the upward outflow interacts with the upper filament branch. Previous simulations have demonstrated turbulence caused by interaction of reconnection outflows with a flux rope and/or with a flare loop top (e.g., Takahashi et al. 2017; Shen et al. 2022).

The large Doppler shifts in the brightening region in this study are not associated with rotational or helical motions of a filament or a jet. The spectra of rotational or helical motions usually have a tilt pattern because the Doppler velocity increases with the distance from the interface between the blue- and redshifts (Rompolt 1975; Curdt et al. 2012). Furthermore, the velocity of rotational or helical motions is typically dozens of km s^{-1} (e.g., De Pontieu et al. 2014b; Yang et al. 2018). In our case, the spectrum manifests a zigzag but not a tilt. Our results show that the velocity is up to the order of 100 km s^{-1} and decreases from the Doppler shift interface (Figure 3).

We have also examined the other three IRIS rasters taken before the partial eruption. Blueshifts of the Si IV 1393.755 Å line between the two filament branches, indicating plausible reconnection outflows, are observed in two later rasters. However, no conclusive counterpart redshifts of the outflows are identified.

4. Analysis of Differential Emission Measure

The temperature, density, and energy in the reconnection region are estimated based on analysis of the differential emission measure (DEM). The DEM is reconstructed with multiple channels of SDO/AIA data using the algorithm provided by Plowman & Caspi (2020). The analysis procedures for the DEM are given in Appendix B. As displayed in Figures 4(a)–(b), the increased emission measure (EM) and EM-weighted temperature (T) are both along the interface between the blue- and redshifts (i.e., the reconnection site), which indicates that plasmas are heated there. The temporal profiles of the DEM and T averaged over four SDO/AIA pixels near the reconnection site are plotted in Figure 4(c). T reaches the peak (~$10^{7.15}$ K, 14 MK) around 22:44 UT when the reconnection and the splitting occur (see Figure 1–2), and drops instantly to the pre-event level after the events. The background temperature is ~$10^{6.68}$ K (4.8 MK), which is from averaging $\log_{10}(T)$ before the peak (see the dashed line in Figure 4(c)). The increment of T during the reconnection is $\Delta T \approx 9.2$ MK.

The EM is also averaged over the four pixels to estimate the density, which peaks at the same time as T. With a mean EM

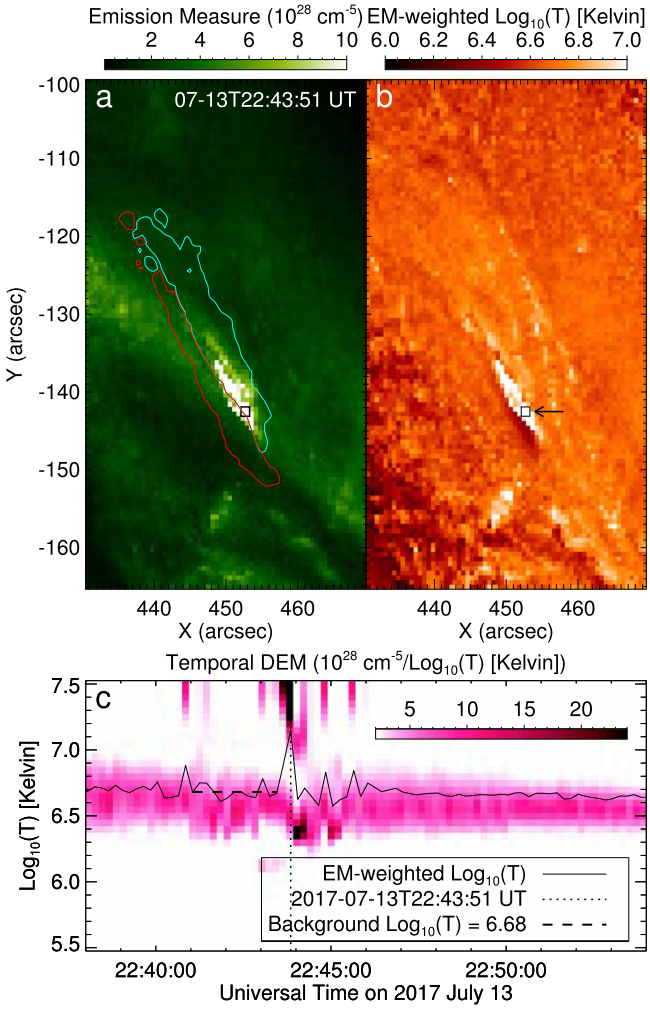

Figure 4. Differential emission measure (DEM) and emission measure (EM) of the reconnection region based on SDO/AIA observations. (a) The EM that is the zeroth moment of DEM. (b) The EM-weighted temperature, which is the first moment of DEM divided by EM. (c) The temporal changes in the DEM that is averaged over the four pixels specified by the square in (b). The field of view of (a)–(b) is similar to that of Figure 2(c)–(e). The contours in (a) are the same as those in Figure 2(b). In (c), the solid curve is the EM-weighted temperature corresponding to the DEM, the dashed line denotes the averaged background EM-weighted temperature (with its span representing the time range 22:41:03–22:43:27 UT), and the dotted line marks the peak time of the EM and EM-weighted temperature.

(~4.67×10^{28} cm^{-5}) before the reconnection, the electron density is estimated to be $n_e \approx 1.94 \times 10^{10}$ cm^{-3}, by assuming a scale for the depth along the line of sight (~1.2×10^{8} cm; see Appendix B for the details). With the peak EM of ~1.92×10^{29} cm^{-5}, the peak electron density is estimated to be ~3.94×10^{10} cm^{-3}. The thermal energy density is $E_{th} \approx 74.7$ ergs cm^{-3}, which is obtained with $n_e \approx 1.94 \times 10^{10}$ cm^{-3} and $\Delta T \approx 9.2$ MK. An ion velocity $v_i \approx 100$ km s^{-1} is taken from the spectroscopic results to calculate the kinetic energy density, which is $E_k \approx 2.06$ ergs cm^{-3}. The ratio of $E_{th}/E_k \approx 36$ indicates that the kinetic energy output is ignorable in this event. Note that the line-of-sight ion velocity given by the spectroscopy could be ~150 km s^{-1} (see Figure 3(d)). Because the reconnection region is ~450″ from the disk center, the actual velocity could be up to ~200 km s^{-1} considering the projection effect and the uncertainty of the velocity direction. If v_i is ~200 km s^{-1}, E_k and E_{th}/E_k can be ~8.25 erg cm^{-3} and ~9, respectively. To estimate the total increased thermal energy

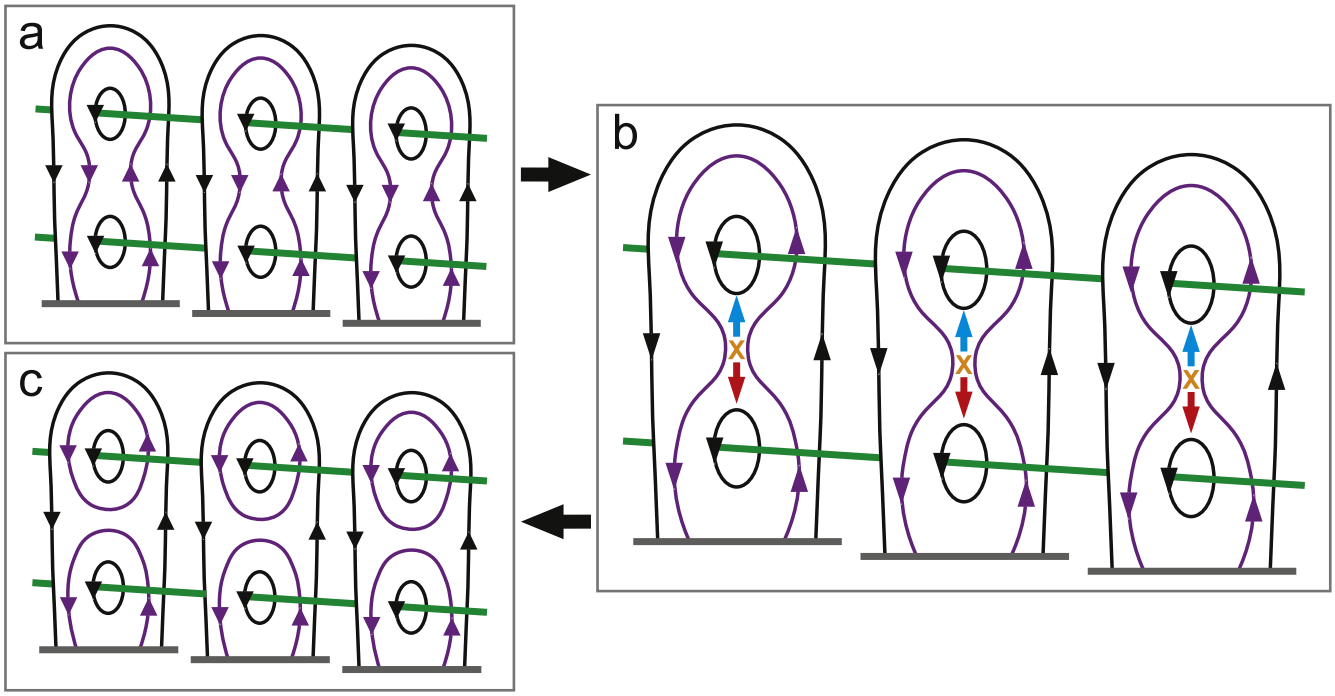

Figure 5. Sketch of the magnetic field lines associated with the reconnection in the filament splitting. (a) Before the reconnection the upper and lower filament branches (green lines) are tethered by the magnetic field lines (purple curves). (b) (enlarged view) Magnetic reconnection occurs at a series of "X" points between the two filament branches, where the blue and red arrows indicate the upward and downward outflows, respectively. (c) After the reconnection the tether magnetic field lines are cut and the filament structure is split.

$W_{\rm th}$, we assume that the heated plasmas are in a cylinder lying in the reconnection region. Then $W_{\rm th} \approx 1.3 \times 10^{27}$ ergs is obtained. The total thermal energy $W_{\rm th}$, the electron density (in the order of 10^{10} cm^{-3}), and the length of the reconnection region ($\sim$14,000 km) are comparable to those of transient brightenings and nanoflares (see Chapter 9 of Aschwanden 2005). The peak electron density $\sim 3.94 \times 10^{10}$ cm^{-3} is not used to calculate the energy, but it does not essentially affect the order-of-magnitude estimate. The orders of magnitude of the derived density and energy are reasonable. However, the derived quantities are dependent on the assumptions of spatial scales (detailed in Appendix B) and could have significant uncertainties. Despite the transient high temperature, we have not seen clear Fe XXI 1354.067 Å profiles during the reconnection.

5. Conclusions and Discussions

We have investigated a magnetic reconnection inside a solar filament structure, using spectroscopic and imaging data from IRIS and SDO. The bidirectional outflows from the reconnection site distribute in an extended region with a length of no less than 14,000 km on the Sun. The velocity of the outflows are $\sim$100 km s^{-1} and decreases remarkably beyond the reconnection site. The temperature in the reconnection region is over 10 MK, which is estimated based on the differential-emission-measure (DEM) analysis. The reconnection splits the filament structure into two upper and lower branches. The filament structure eventually erupted partially, with the upper branch ejected and the lower branch retained.

The unprecedented extent of the reconnection region implies an extended reconnection of a series of magnetic field lines in the filament structure (see the cartoon in Figure 5). The extent is comparable to the horizontal length of the current sheet obtained in three-dimensional magnetohydrodynamic simulations (e.g., Jiang et al. 2021; Shen et al. 2022). Our study also shows unambiguous spectroscopic evidence for the splitting of a filament structure by magnetic reconnection. The reconnection in the extended region cuts the magnetic field lines binding the two filament branches (Figure 5), after which the upper branch rises (Figure 1(g)). This is reminiscent of the "tether-cutting" model (Moore et al. 2001), and provides a mechanism for forming a "double-decker" filament structure (Liu et al. 2012). Interaction between the upward outflow and the upper filament branch is inferred from the line broadening far from the reconnection site (Figure 3), which may be responsible for the rise of the upper branch. The upward reconnection outflow is also suggested to push the upper flux rope in a recent simulation of solar eruptions (Jiang et al. 2021).

The temperature of the reconnection region shows a transient increase to above 10 MK, which is in the order of those of large flares, although the total thermal energy output ($\sim 10^{27}$ ergs) is several orders of magnitude lower than those of large flares. The total thermal energy dominates the kinetic energy in this event, which is generally consistent with simulations (e.g., Aunai et al. 2011; Shu et al. 2021). However, energy partition in magnetic reconnection with a similar energy level is still in debate (e.g., Inglis & Christe 2014; Warmuth & Mann 2020).

The filament structure finally erupted partially by ejecting the upper branch, and the lower branch remained (see Figure 1 and animation). The splitting and partial eruption of a filament may contribute to successive coronal mass ejections from the same active region (e.g., Birn et al. 2006; Cheng et al. 2018), which are more likely to bring severe geomagnetic effects than a single ejection (Liu et al. 2014; Lugaz et al. 2017). Indeed, 9 days later the same active region as in our case produced multiple filament ejections, which caused a surprising magnetic field at 1 au as high as 68 nT (Liu et al. 2019).

This Letter has provided definite spectroscopic evidence for the splitting of a filament structure by magnetic reconnection, and has presented a new view on the spatial distribution of the outflows and the thermal properties of reconnection.

We thank Dr. Yajie Chen, Dr. Leping Li, Dr. Rui Wang, and Prof. Xin Cheng, for their valuable suggestions and discussions. We are grateful to the anonymous referee for constructive comments. The research is supported by the National Natural Science Foundation of China (grants No. 42004145, 42274201, 42150105, and 11733003), the Major Project of Chinese National Programs for Fundamental Research and Development (grant No. 2021YFA0718600), the CAS Strategic Priority Program on Space Science (grant No. XDA15018500), and the Specialized Research Fund for State Key Laboratories of China. H.H. is also supported by CSC (grant No. 201804910106) and MPS. L.P.C. gratefully acknowledges funding by the European Union (grant agreement No. 101039844). Views and opinions expressed are however those of the author(s) only and do not necessarily reflect those of the European Union or the European Research Council. Neither the European Union nor the granting authority can be held responsible for them. IRIS is a NASA small explorer mission developed and operated by LMSAL with mission operations executed at NASA Ames Research Center and major contributions to downlink communications funded by ESA and the Norwegian Space Centre. SDO is the first mission launched for NASA's Living With a Star Program. We acknowledge the use of data from GOES-15.

Facilities: IRIS, SDO, GOES-15.

Software: MPFIT (Markwardt 2009), simple_reg_dem (Plowman & Caspi 2020), SolarSoftWare (Freeland & Handy 2012).

Appendix A
Spectroscopic Analysis of IRIS Data

A single Gaussian function with a continuum, $I(v) = A \cdot \exp[-\frac{(v-v_D)^2}{w_{1/e}^2}] + c$, is used to fit the line profiles, where v is the given wavelength in Doppler shift units of kilometers per second, and A, v_D, $w_{1/e}$, and c are free parameters for the peak intensity, Doppler velocity, 1/e width, and continuum, respectively (Peter 2010). The nonthermal width w_{nt} in Figure 2(d) is determined by $w_{nt} = \sqrt{w_{1/e}^2 - w_{th}^2 - w_{instr}^2}$, where w_{th} is the thermal width 6.63 km s^{-1} corresponding to the formation temperature 80,000 K for Si IV 1393.755 Å line, and w_{instr} is the instrumental width 6.46 km s^{-1} for spectral resolution 0.05 Å. The total intensity in Figure 2(e) is calculated with $I_{tot} = \sqrt{\pi} \cdot A \cdot w_{1/e}$. Near the reconnection site, some Si IV line profiles have two Gaussian components, and a double Gaussian function with a continuum is employed to fit these profiles (see Figure 3). The fittings are performed using the routine `mpcurvefit.pro` in the SolarSoftWare (SSW; available at https://www.lmsal.com/solarsoft) provided by Markwardt (2009). The uncertainties in Figures 3(c)–(d) are the 1σ errors given by the routine.

The Doppler velocities in this study are calibrated by removing the Doppler shift of the chromospheric Fe II 1392.817 Å line (Tian et al. 2018). To get the Doppler shift, the Fe II line profile is averaged over all spatial pixels in the raster, and then is fitted by a single Gaussian function as described above. The Doppler shift of Fe II 1392.817 Å line is ~1 km s^{-1}, which is consistent with the fact that the cold line velocity is usually trivial (Peter et al. 2014; Tian et al. 2018).

An IRIS Mg II k wing image has similar bright features to an SDO/AIA 1700 Å image (Chen et al. 2019). We cross-correlate these two types of images to align coordinates of IRIS rasters to those of SDO images. An AIA 1700 Å image, whose observation time (22:43:40 UT on 2017 July 13) is during the reconnection, is first cropped to the field of view of the IRIS raster. The Mg II k wing image is made by summing the intensities at wavelengths of 2796.352 + 1.33 Å and 2796.352 − 1.33 Å, and then resampled to the resolution of the AIA 1700 Å image. The shift between the Mg II k wing and AIA 1700 Å images are computed by the routine `malign.pro` in SSW. Finally, a shift of (2″, 3″) in X and Y directions is given and is adjusted to the coordinates of the IRIS maps in Figure 2.

Appendix B
Differential Emission Measure Based on SDO/AIA Data

The differential emission measure (DEM) is obtained using the code `simple_reg_dem.pro` in SSW provided by Plowman & Caspi (2020). Six channels (94, 131, 171, 193, 211, and 335 Å) of coaligned SDO/AIA images are the input. The output DEM is of per unit $\log_{10}(T)$, where $\log_{10}(T)$ is the logarithm of temperature T in kelvins. The emission measure (EM) is given by $EM = \int DEM(T_{log}) dT_{log}$, where $T_{log} = \log_{10}(T)$ ranges from 5.5 to 7.5 with a step of 0.05. The logarithm of EM-weighted temperature is $\overline{T}_{log} = \int DEM(T_{log}) T_{log} dT_{log} / EM$ (for details see Plowman & Caspi 2020).

The electron density is $n_e = \sqrt{EM/l}$, where l is the depth along the line of sight. The depth $l \approx 1.2 \times 10^8$ cm is assumed to be equivalent to the width of the region with enhanced EM and EM-weighted temperature (see Figure 4(a)-(b)). The thermal energy density is obtained with $E_{th} = 3 n_e k_B \Delta T$, where k_B is the Boltzmann constant and ΔT is the increased EM-weighted temperature. The kinetic energy density is calculated with $E_k = \frac{1}{2} \mu m_H n_e v_i^2$, where $\mu \approx 1.27$ is the mean molecular weight (see Chapter 3 of Aschwanden 2005), m_H is the hydrogen mass, and $v_i \approx 100$ km s^{-1} is the ion velocity estimated from the Si IV line Doppler shift. Assuming that the heated plasmas are in a cylinder volume V, the total thermal energy is given by $W_{th} = E_{th} V$. The cylinder height and diameter are $\sim 1.4 \times 10^9$ cm (the distance between the two crosses ("+") in Figure 2(e)) and $\sim 1.2 \times 10^8$ cm (the depth along the line of sight), respectively.

ORCID iDs

Huidong Hu https://orcid.org/0000-0001-8188-9013
Ying D. Liu https://orcid.org/0000-0002-3483-5909
Lakshmi Pradeep Chitta https://orcid.org/0000-0002-9270-6785
Hardi Peter https://orcid.org/0000-0001-9921-0937
Mingde Ding https://orcid.org/0000-0002-4978-4972

References

Antolin, P., Pagano, P., Testa, P., Petralia, A., & Reale, F. 2021, NatAs, 5, 54
Antonucci, E., Rosner, R., & Tsinganos, K. 1986, ApJ, 301, 975
Aschwanden, M. J. 2005, Physics of the Solar Corona: An Introduction with Problems and Solutions (Berlin: Springer)
Aunai, N., Belmont, G., & Smets, R. 2011, PhPl, 18, 122901
Birn, J., Forbes, T. G., & Hesse, M. 2006, ApJ, 645, 732
Chen, Y., Tian, H., Zhu, X., et al. 2019, ScChE, 62, 1555
Cheng, X., Kliem, B., & Ding, M. D. 2018, ApJ, 856, 48

Chifor, C., Young, P. R., Isobe, H., et al. 2008, A&A, 481, L57
Chitta, L. P., & Lazarian, A. 2020, ApJL, 890, L2
Curdt, W., Tian, H., & Kamio, S. 2012, SoPh, 280, 417
De Pontieu, B., Rouppe van der Voort, L., McIntosh, S. W., et al. 2014b, Sci, 346, 1255732
De Pontieu, B., Title, A. M., Lemen, J. R., et al. 2014a, SoPh, 289, 2733
Dudík, J., Polito, V., Dzifčáková, E., Del Zanna, G., & Testa, P. 2017, ApJ, 842, 19
Freeland, S. L., & Handy, B. N. 2012, SolarSoft: Programming and Data Analysis Environment for Solar Physics, Astrophysics Source Code Library, record ascl:1208.013
French, R. J., Matthews, S. A., van Driel-Gesztelyi, L., Long, D. M., & Judge, P. G. 2020, ApJ, 900, 192
Gibson, S. E., & Fan, Y. 2006, ApJL, 637, L65
Gilbert, H. R., Holzer, T. E., & Burkepile, J. T. 2001, ApJ, 549, 1221
Goldstein, M. L., Matthaeus, W. H., & Ambrosiano, J. J. 1986, GeoRL, 13, 205
Gordovskyy, M., Kontar, E. P., & Browning, P. K. 2016, A&A, 589, A104
Hong, J., Ding, M. D., Li, Y., et al. 2016, ApJL, 820, L17
Hu, H., Liu, Y. D., Zhu, B., et al. 2019, ApJ, 878, 106
Inglis, A. R., & Christe, S. 2014, ApJ, 789, 116
Innes, D. E., Inhester, B., Axford, W. I., & Wilhelm, K. 1997, Nat, 386, 811
Jeffrey, N. L. S., Fletcher, L., Labrosse, N., & Simões, P. J. A. 2018, SciA, 4, 2794
Jiang, C., Feng, X., Liu, R., et al. 2021, NatAs, 5, 1126
Jing, J., Inoue, S., Lee, J., et al. 2021, ApJ, 922, 108
Kliem, B., Török, T., Titov, V. S., et al. 2014, ApJ, 792, 107
Lemen, J. R., Title, A. M., Akin, D. J., et al. 2012, SoPh, 275, 17
Li, D., Li, L., & Ning, Z. 2018, MNRAS, 479, 2382
Lin, J., Raymond, J. C., & van Ballegooijen, A. A. 2004, ApJ, 602, 422
Liu, R., Gilbert, H. R., Alexander, D., & Su, Y. 2008, ApJ, 680, 1508
Liu, R., Kliem, B., Török, T., et al. 2012, ApJ, 756, 59
Liu, Y. D., Luhmann, J. G., Kajdič, P., et al. 2014, NatCo, 5, 3481
Liu, Y. D., Zhao, X., Hu, H., Vourlidas, A., & Zhu, B. 2019, ApJS, 241, 15
Lugaz, N., Temmer, M., Wang, Y., & Farrugia, C. J. 2017, SoPh, 292, 64
Markwardt, C. B. 2009, in ASP Conf. Ser. 411, Astronomical Data Analysis Software and Systems XVIII, ed. D. A. Bohlender, D. Durand, & P. Dowler (San Francisco, CA: ASP), 251
Martin, S. F. 1998, SoPh, 182, 107
Moore, R. L., Sterling, A. C., Hudson, H. S., & Lemen, J. R. 2001, ApJ, 552, 833
Ortiz, A., Hansteen, V. H., Nóbrega-Siverio, D., & Rouppe van der Voort, L. 2020, A&A, 633, A58
Pesnell, W. D., Thompson, B. J., & Chamberlin, P. C. 2012, SoPh, 275, 3
Peter, H. 2010, A&A, 521, A51
Peter, H., Tian, H., Curdt, W., et al. 2014, Sci, 346, 1255726
Plowman, J., & Caspi, A. 2020, ApJ, 905, 17
Polito, V., Galan, G., Reeves, K. K., & Musset, S. 2018, ApJ, 865, 161
Rompolt, B. 1975, SoPh, 41, 329
Scherrer, P. H., Schou, J., Bush, R. I., et al. 2012, SoPh, 275, 207
Shen, C., Chen, B., Reeves, K. K., et al. 2022, NatAs, 6, 317
Shu, Y., Lu, S., Lu, Q., Ding, W., & Wang, S. 2021, JGRA, 126, e29712
Takahashi, T., Qiu, J., & Shibata, K. 2017, ApJ, 848, 102
Tian, H., Zhu, X., Peter, H., et al. 2018, ApJ, 854, 174
Tripathi, D., Gibson, S. E., Qiu, J., et al. 2009, A&A, 498, 295
Warmuth, A., & Mann, G. 2020, A&A, 644, A172
Yang, Z., Tian, H., Peter, H., et al. 2018, ApJ, 852, 79
Zweibel, E. G., & Yamada, M. 2009, ARA&A, 47, 291